

Theodore Zirkle¹

Woodruff School of Mechanical Engineering,
Georgia Institute of Technology,
Atlanta, GA 30332
e-mail: tzirkle6@gatech.edu

Luke Costello

Woodruff School of Mechanical Engineering,
Georgia Institute of Technology,
Atlanta, GA 30332
e-mail: lcostello@ab.mpg.de

Ting Zhu

Woodruff School of Mechanical Engineering,
Georgia Institute of Technology,
Atlanta, GA 30332
e-mail: ting.zhu@me.gatech.edu

David L. McDowell

Woodruff School of Mechanical Engineering,
Georgia Institute of Technology,
Atlanta, GA 30332
e-mail: david.mcdowell@me.gatech.edu

Modeling Dislocation-Mediated Hydrogen Transport and Trapping in Face-Centered Cubic Metals

The diffusion of hydrogen in metals is of interest due to the deleterious influence of hydrogen on material ductility and fracture resistance. It is becoming increasingly clear that hydrogen transport couples significantly with dislocation activity. In this work, we use a coupled diffusion-crystal plasticity model to incorporate hydrogen transport associated with dislocation sweeping and pipe diffusion in addition to standard lattice diffusion. Moreover, we consider generation of vacancies via plastic deformation and stabilization of vacancies via trapping of hydrogen. The proposed hydrogen transport model is implemented in a physically based crystal viscoplasticity framework to model the interaction of dislocation substructure and hydrogen migration. In this study, focus is placed on hydrogen transport and trapping within the intense deformation field of a crack tip plastic zone. We discuss the implications of the model results in terms of constitutive relations that incorporate hydrogen effects on crack tip field behavior and enable exploration of hydrogen embrittlement mechanisms. [DOI: 10.1115/1.4051147]

Keywords: hydrogen transport, hydrogen trapping, hydrogen embrittlement, crystal plasticity, finite element analysis, constitutive relations, elastic behavior, environmental effects, fracture, mechanical behavior, microstructure property relationships, plastic behavior

1 Introduction

Literature regarding the influence of hydrogen (H) on metals dates back to 1875 [1]. Many subsequent experimental and theoretical studies have investigated the effects of H on the mechanical response of metals [2]. Complete understanding remains elusive despite this rich history of investigation, and resolution of the problem remains desirable due to the common exposure of structural metals to H in a variety of energy applications [3,4].

Hydrogen fundamentally changes the effective response of a material, most frequently causing components to exhibit loss of ductility and increasing susceptibility to fatigue failure [5]. Lower length scale investigations often reveal more complex interactions between H and the host material, e.g., competition between material hardening and softening [6]. To effectively design for the influence of H based on a broad range of experimental observations, a wide variety of mechanisms have been proposed. The most commonly cited mechanisms include hydride precipitation, hydrogen enhanced localized plasticity [7,8], adsorption induced dislocation emission [9–12], hydrogen enhanced decohesion [13,14], and hydrogen enhanced strain induced vacancy creation [15,16]. While each mechanism has a reasonable basis, experimental investigations are typically based on averaged, macroscale behavior, precluding direct observation of the proposed mechanism(s) at appropriately small length and time scales. Therefore, accurate computational modeling at operative sub-micron length scales is key to elucidating the governing processes.

Regardless of the mechanism(s) subscribed to, the deleterious effects of H are directly linked to the elevated concentration of H in small volumes of material in critically stressed or strained regions such as notches and crack tips. Faithful representation of

the H distribution is prerequisite to more complete consideration of the mechanistic aspects of hydrogen embrittlement. Computational simulations of H transport and trapping are therefore essential. Sofronis and McMeeking [17] considered the distribution of H ahead of a crack tip, accounting for diffusion driven by the H chemical potential. This approach has been adopted by a number of researchers in a variety of computational frameworks [18–22]. These works, applicable to length scales well above those of dislocation substructure, do not capture important mesoscale transport and trapping processes. These processes, affected by the evolution of certain material defect populations, have been experimentally observed to increase the rate of H transport. Saintier et al. [23] found enhanced H transport at a crack tip in face-centered cubic (FCC) stainless steel, attributed to dislocation-mediated processes due to the lack of appreciable martensitic transformation. Dislocation transport processes were partially accounted for in the recent computational work of Dadfarnia et al. [24] via introduction of the convective transport of H via mobile dislocations. Dadfarnia et al. [24] found that accounting for this mechanism enhanced the H transport, supporting the notion that mesoscale transport processes play an important role in the overall distribution of H at sufficiently small length scales. This paper extends the current state-of-the-art computational H transport framework to more comprehensively account for a variety of line and point defect populations and their influence on the distribution of H ahead of a crack tip in an FCC metal.

2 Hydrogen Transport

2.1 Mesoscopic H Transport Mechanisms. As noted in the experimental observations of Murakami et al. [25] and Nagumo [16], dislocations and vacancies (V_a) play an important role in the H distribution problem. As such, we consider mobile dislocations, dislocation wall substructures, and V_a to be among possible H traps. Grain boundaries are not considered in this treatment. We label the H concentration according to respective sites, namely, in the lattice C_L , at mobile dislocations C_{HMD} , at

¹Corresponding author.

Contributed by the Materials Division of ASME for publication in the JOURNAL OF ENGINEERING MATERIALS AND TECHNOLOGY. Manuscript received January 5, 2021; final manuscript received May 6, 2021; published online May 31, 2021. Assoc. Editor: David Field.

dislocation wall substructures C_{HWD} , and trapped in H-Va complexes C_{HVa} . Furthermore, we label the mobile H concentration C_M and the total H concentration C_H .

Estimation of the H distribution via computational techniques requires knowledge of operative H transport mechanisms. As discussed, these include mechanisms commonly addressed, such as H diffusion driven by the chemical potential, i.e., the lattice concentration gradient [17,26] and hydrostatic stress gradient [27,28]. Furthermore, we consider additional transport mechanisms that operate on the mesoscale; these include pipe diffusion of H along the cores of edge dislocations [29,30] and sweeping of H through the lattice via migration of mobile screw dislocations [24,26,31,32]. These various modes of H transport are important to consider at appropriate length scales as dislocations play a role in H transport [32]. Dislocation-mediated transport mechanisms operate on different components of the overall H concentration. Namely, the dislocation pipe diffusion mechanism is related to C_{HWD} , while the convective dislocation sweeping mechanism is related to C_{HMD} .

As a first-order approximation, it is assumed that the time scales required for significant time-dependent relaxation of sessile dislocation structures and diffusion of Va are much longer than the time scales required for H diffusion [33]. Sweeping of H by mobile dislocations does not fall into this category and must be considered. Furthermore, strain-induced Va are considered to be strong traps for H while mobile screw and wall edge dislocations are considered to be relatively weak traps by comparison. This approximation is justified from a thermodynamic perspective when considering the binding energy of each trap type. In nickel, the hydrogen-dislocation binding energy has been found to be between 0.04 and 0.13 eV [34,35], and the hydrogen-vacancy binding energy proposed to be between 0.27 and 0.44 eV [36,37]. Overall, the literature values vary slightly, but the trends are consistent; H-Va binding energies are four to six times greater than H-dislocation binding energies.

Considering Va to be the strongest trap in the system is further justified from a kinetics/mobility perspective. The interaction distance of a dislocation with its impurity field can be estimated as $30b$ where b is the Burgers vector [38]. This distance is significantly larger than the spatial variation in background electron density associated with vacancy trap sites, on the order of b . As such, we treat vacancies as relatively localized traps when compared with the more diffuse nature of dislocation trapping sites. The diffuse nature of H-dislocation binding sites, along with lower binding energies, supports their treatment as relatively weak traps, with H having higher probability to exit the trap. Both thermodynamic and kinetic arguments are qualitatively depicted in Fig. 1, where E_0 is the energy of H in the lattice, E_{disl} is the energy of H in a dislocation, E_{Va} is the energy of H in Va, and r is the distance from the trap of interest. The factor of 5 shown in the equation in Fig. 1 results from the ratio of H-Va binding energy to H-dislocation binding energy, as reviewed in the preceding paragraph.

The foregoing argument implies that H is not “trapped” at edge or screw dislocations per se, but rather is subject to different transport mechanisms compared with H in the lattice C_L . H resident in edge dislocation cores C_{HWD} is subject to pipe diffusion, whereas H ensnared by screw dislocation segments C_{HMD} is subject to transport via dislocation sweeping. By comparison, we consider that

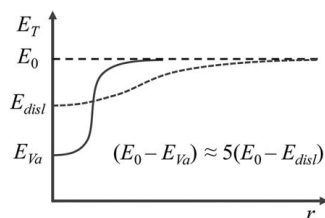


Fig. 1 Trap binding energy as a function of distance from the trap

H-Va complexes are stable despite interaction with mobile dislocations based on atomistic simulations by Li et al. [39] in iron. These considerations imply that the mobile C_M and total H concentration C_H can be described as $C_M = C_L + C_{HWD} + C_{HMD}$ and $C_H = C_M + C_{HVa}$, respectively. The arguments outlined above can be summarized via three governing assumptions:

- Mobile screw dislocations and edge wall dislocations weakly trap H, i.e., do not “lock” H in place. Weak traps are also considered to be diffuse and H can escape to encounter a different type of trap.
- Va strongly trap H and inhibit further diffusion; the rate of Va diffusion is also significantly reduced.
- Weak and strong traps are each in local equilibrium with lattice H, and traps do not interact with each other.

2.2 Hydrogen Transport Model. The governing continuity equation for H concentration can be written as

$$\frac{\partial C_H}{\partial t} + \nabla \cdot \mathbf{J} = 0 \quad (1)$$

where C_H was defined previously and \mathbf{J} is the flux of H [40]. Proper application of Eq. (1) requires the development of constitutive equations that explicitly consider H trapping and transport. First, partitioning the H trapped at various defects will be addressed. Subsequently, the constitutive equations for the H flux \mathbf{J} will be discussed. Lastly, the effective H diffusivity in the crystal will be considered.

2.3 Hydrogen Trapping. The problem of H trapping has been previously studied [17,24]. To extend these treatments, we follow the framework of Ref. [17] and invoke the governing assumptions associated with the mesoscopic H transport mechanisms identified in Sec. 2.2. Doing so yields simple equilibrium relations between the trapped H concentrations C_T and background mobile concentration C_M , i.e.

$$C_{T=HWD,HMD,HVa} = \frac{\alpha_T N_T C_M K_T}{C_M (K_T - 1) + \beta N_L} \quad (2)$$

where α_T is the number of H atoms per trap site, β is the number of H atoms per normal lattice site, N_T is the number of H traps per reference volume, and K_T is the associated equilibrium constant. The equilibrium constant, K_T , is written as a function of the binding energies for each trap type, i.e., $K_T = \exp(-E_T/RT)$ where R is the universal gas constant, T is the absolute temperature, and E_T is the trap binding energy. Equation (2) is applied for each trap type proposed to be operative in the current case. For dislocations, a “trap site” does not correspond to a single atomic site, but rather a more diffuse region encompassing the region of tensile stress produced by the presence of the dislocation.

The notation used in Eq. (2) and in the definition of C_M requires some clarification as the trapped H concentrations C_{HWD} and C_{HMD} seemingly appear on both sides of Eq. (2). This notation results from the assumed temporal evolution of immobile and mobile H concentrations. Based on our qualitative examination of H-trap binding energies, we expect H trapped by dislocations to have a high probability for trap escape. In other words, at time t , C_M is partitioned among the various trap types. If H is trapped by Va, it is considered to be immobile. On the other hand, if H is trapped by a dislocation, it is considered to remain mobile with a high probability for trap escape. Consequently, at time $t + \Delta t$, the H trapped by dislocations are susceptible to be trapped by other trap types as determined by the H-trap binding energies.

2.4 Hydrogen Flux. Prior H transport frameworks considered the chemical potential as driving H flux through the H concentration and hydrostatic stress gradients [17]. This can be written in terms of the effective lattice diffusivity D_{eff} and mobile components of H

concentration exclusive of C_{HMD} , i.e.

$$J_L = -D_{eff} \nabla (C_L + C_{HWD}) \quad (3)$$

$$J_\sigma = \frac{D_{eff}(C_L + C_{HWD})V_H}{RT} \nabla \sigma_H \quad (4)$$

where σ_H is the hydrostatic stress and V_H is the partial molar volume of H in solid solution. Here, σ_H is defined as the trace of the stress tensor divided by three. These fluxes involve C_L and C_{HWD} , owing to our assumption that pipe diffusion along dislocations enhances the effective lattice diffusivity at the mesoscale.

As discussed, an additional flux term should be included to account for H transport via migration of mobile screw dislocations, as considered in the recent work of Dadfarnia et al. [24]. The H flux attributed to dislocation motion is given by

$$J_D = (N_{HMD} V^D) (\theta_{HMD}) = C_{HMD} V^D \quad (5)$$

where N_{HMD} describes the number of available trap sites at mobile dislocations, V^D is the dislocation velocity vector, and θ_{HMD} describes the number of occupied mobile dislocation traps per total available dislocation traps. The dislocation velocity vector V^D corresponds to the average dislocation velocity considering the dislocation velocity on each slip system obtained via Orowan's equation, i.e., $\bar{v}^\alpha = \dot{\gamma}^\alpha / \rho^\alpha b$. Here, $\dot{\gamma}^\alpha$ and ρ^α are the shearing rate and dislocation density on a particular slip system α and b is the Burgers vector. Due to the dependence of V^D on the dislocation density of each slip system, any dislocation processes such as cross slip accounted for in the accompanying mechanical model are automatically considered here. Combining the flux contributions from H concentration gradient, hydrostatic stress gradient, and dislocation flux yields the expression for H flux as $J = J_L + J_\sigma + J_D$.

2.5 Effective Diffusivity. H diffusion through a deformed crystalline lattice can be enhanced via the high diffusivity pathways associated with dislocation cores, previously discussed as pipe diffusion [29]. The effective diffusivity in the presence of pipe diffusion has been accounted for with rule of mixture approximations [41] as $D_{eff} = (1 - f_d)D_L + f_d D_{PD}$. Here, f_d is the volume fraction of dislocation cores, D_L is the lattice diffusivity, and D_{PD} is the dislocation core diffusivity. As explained by Chen and Schuh [42], the rule of mixtures approach does not capture the geometric complexity of random dislocation networks. Chen and Schuh [42] invoked percolation theory to justify raising the f_d term to a positive power in order to reduce the idealized rule of mixtures diffusivity to account for the path tortuosity of random dislocation distributions. When considering nonrandom, ordered dislocation structures, however, it is difficult to justify the use of a similar power scaling value from percolation theory. In moderate to highly strained crystals, dislocation substructures develop, and these structures are highly ordered and interconnected, i.e., past the critical percolation limit. Additionally, previous literature [43] has proposed that dislocation networks are always at the percolation limit given that they cannot terminate in a perfect crystal.

As opposed to applying the lattice and pipe diffusion diffusivities to individual H populations, the high probability for trap escape prompts an averaged approach utilizing an effective diffusivity D_{eff} . As such, we adopt a rule of mixtures assignment, where the pipe and lattice diffusivities are weighted by the associated H concentration fractions, i.e.

$$D_{eff} = \frac{C_L}{C_M - C_{HMD}} D_L + \frac{C_{HWD}}{C_M - C_{HMD}} D_{PD} \quad (6)$$

2.6 Parameter Estimation. Application of the H transport framework in the example system, nickel, requires the estimation of several parameters. First, considering the number of dislocation traps in Eq. (2), we follow the assumption that there is one trap per atomic plane threaded by a dislocation [44,45], i.e.,

$N_T = \sqrt{3} \rho_T / a$. Here, the factor $\sqrt{3}$ is related to the FCC lattice, a is the lattice parameter, the subscript T denotes the type of dislocation trap, and ρ_T is the dislocation density as calculated by the crystal plasticity model. The number of Va traps is more complicated to estimate and will be presented in Sec. 2.7 as an extension to an existing crystal plasticity framework.

Next, the trap binding energies are considered. The binding energy of H to Va in nickel is defined to be 0.44 eV as measured by Fukai [46]. Following Kocks et al. [47], we assign the bulk of mobile dislocations to be of screw character, prompting the assignment of the binding energy of H to mobile dislocations to be 0.07 eV, a simple average of the values calculated by Angelo et al. [35] and Wen et al. [34]. Under the assumption that the majority of wall dislocations are of edge character, as outlined by Mughrabi [48], we assign the value of the binding energy of H to wall dislocations to be 0.115 eV, again an average of the values calculated by Angelo et al. [35] and Wen et al. [34].

Subsequently, we estimate diffusivity values by first presenting the general form of the temperature dependence of diffusion, written as $D = D_0 \exp(-H_D/RT)$ where D_0 is the diffusion coefficient and H_D the activation energy for diffusion. For H in bulk nickel, D_0 and H_D were measured by Louthan et al. [49] as $7.0 \times 10^{-7} \text{ m}^2/\text{s}$ and 39.6 kJ/mol, respectively, with similar values being found by other researchers [50]. The estimation of the parameters governing H diffusion in a dislocation core is more difficult due to the lack of data in the literature. However, based on preliminary embedded atom method (EAM) calculations [51], the activation energy for screw dislocation core diffusion was found to decrease on the order of 1.6 relative to the lattice; edge dislocations would likely result in even greater decreases for core diffusion. Pending more accurate calculations, D_0 and H_D for pipe diffusion are set to be $7.0 \times 10^{-7} \text{ m}^2/\text{s}$ and 24.7 kJ/mol, respectively. The diffusivity is relatively sensitive to the value of H_D due to the exponential dependence, and the H_D values described above are considered as characteristic values. Any deviations in these values would be expected to scale the flux components driven by the chemical potential gradient, and the expected change in response can be guided by the discussion related to Figs. 8 and 10.

The number of H atoms resident per trap depends on the type of trap considered. Following Liang et al. [52], we consider an atmosphere of H atoms trapped in the tensile region of the stress field associated with a dislocation and assign the value of α_T in Eq. (2) to be 10 for both mobile and wall dislocation traps. With regard to Va traps, Zheng et al. [53] suggests a value of six H atoms per Va, with other researchers suggesting similar values [37,54]. We consider these approximations to be appropriate for a mesoscopic model.

2.7 H Transport Model Summary. Overall, the H transport model partitions the H concentration into weakly trapped, mobile (C_{HWD} , C_{HMD}) and strongly trapped, immobile H concentrations (C_{HVa}) according to H-trap binding energies. Subsequently, the partitioned H concentrations are used to calculate the quantities required to solve the H transport continuity equation. The influence

Table 1 Transport mechanisms and proposed equations for the H transport problem

Transport mechanism	Proposed equation
Chemical potential gradient	$J_L = -D_{eff} \nabla (C_L + C_{HWD})$
Hydrostatic stress gradient	$J_\sigma = \frac{D_{eff}(C_L + C_{HWD})V_H}{RT} \nabla \sigma_H$
Mobile screw dislocation sweeping/convection	$J_D = C_{HMD} V^D$
Edge dislocation pipe diffusion	$D_{eff} = \frac{C_L}{C_M - C_{HMD}} D_L + \frac{C_{HWD}}{C_M - C_{HMD}} D_{PD}$

Table 2 H transport model parameters for nickel

Property	Symbol	Ni
Dislocation trap number	N_{HWD}, N_{HMD}	$\sqrt{3}\rho_T/a$
Lattice site number	N_L	$1/V_M$
Lattice parameter	a	0.352 nm
Binding energy to mobile dislocations	E_{HMD}	0.07 eV
Binding energy to wall dislocations	E_{HWD}	0.115 eV
Binding energy to Va	E_{HVa}	0.44 eV
Lattice diffusivity (300 K)	D_L	$9.27 \times 10^{-14} \text{ m}^2/\text{s}$
Dislocation core diffusivity (300 K)	D_{PD}	$3.50 \times 10^{-11} \text{ m}^2/\text{s}$
Sites per dislocation trap	$\alpha_{HWD}, \alpha_{HMD}$	10
Sites per Va trap	α_{HVa}	6
Sites per host atom	β	1
Partial molar volume of H	V_H	$2 \times 10^{-6} \text{ m}^3/\text{mol}$
Molar volume of host lattice	V_M	$6.59 \times 10^{-6} \text{ m}^3/\text{mol}$

of each mechanism on the transport of H is outlined in Table 1. The values used in the application of the model for nickel at 300 K are outlined in Table 2.

3 Application of the Hydrogen Transport Model

3.1 Crystal Plasticity Model. Implementation of the H transport model requires relatively detailed information at the length scale of self-organized dislocation substructure, which is generally somewhat below the spacing of integration points in the corresponding finite element model. The MS-CP model developed by Castelluccio and McDowell [55] is used to couple stress and deformation with H transport in single crystals. This model uses a multiplicative decomposition of the deformation gradient and a Kocks-Argon-Ashby thermal-activation type flow rule [47]. The model incorporates microscale and mesoscale mechanisms and is informed by bottom-up simulations and lower length scale as well as laboratory specimen-scale experiments. This model is ideal for use with the proposed mesoscopic H transport framework because it explicitly models the evolution of defect densities and dislocation substructure while simultaneously limiting phenomenological approximations, improving its capabilities to predict transient processes near notches and crack tips.

The crystal plasticity model was calibrated to experimental data from a nickel single crystal loaded along the $\langle -167 \rangle$ direction to 7% strain [56], as shown in Fig. 2. Full constitutive modeling and parameterization details for the MS-CP model appear in the paper

devoted to the development of the model [55], and a brief overview of constitutive details is provided in the Appendix.

While the MS-CP model describes the evolution of both dislocation density and substructure, the H transport model requires estimation of the excess Va traps produced during plastic deformation. To this end, we extend the MS-CP model to include Va generation. Nonequilibrium Va concentrations significantly higher than typical equilibrium lattice concentrations are often observed in metals at high plastic strains. Production of large numbers of Va is believed to be associated with the activity of dislocations [57,58], which are then stabilized by H [46], acting to lower the Va formation energy. One particular model ascribes the production of excess Va to dislocation activity via persistent slip bands (PSBs), based on a previously developed dislocation bowing and passing model [59–61]. In a PSB, planar dislocation rich walls are separated by dislocation sparse channels. Under an applied stress, dislocation loops may bow out from the walls into the channels. The loops can cross the channel completely, with the leading-edge segment being absorbed into the adjacent wall, leaving behind two screw segments spanning the channel. Alternatively, if two opposite sign loops come within some annihilation distance of each other, the leading-edge segments will annihilate, forming a row of point defects. This process will leave behind two jogged screw segments spanning the channels. These segments can then move away from each other, leaving behind a line of point defects created by the nonconservative dragging of the jogs.

Polák and Sauzay [58] proposed a model for the balance of Va concentration in PSBs. In their model they take the Va production rate to be independent of the current Va concentration and the Va annihilation rate to be a linear function of the current Va concentration, i.e., $\partial C_{Va}/\partial N = p - AC_{Va}$, where p is the production rate parameter, A is the annihilation parameter, C_{Va} is the Va concentration, and N is the cycle number. They then calculate the Va concentration as $C_{Va} = p/A(1 - \exp(-AN))$.

While this approach is appealing in its simplicity, the production and annihilation parameters are unclear. In the following, we propose a model in the spirit of the work of Polák and Sauzay [58], but directly account for the statistics of the dislocation bow out processes.

To more clearly define the Va production term, we consider the statistics of dislocation bow out and annihilation processes. Following the approach of Davoudi and Vlassak [62], we consider a collection of sources with their activation strengths being normally distributed. If the probability density for the source strength, Ψ^α , obeys a normal distribution, then the cumulative distribution function on slip system α is given by

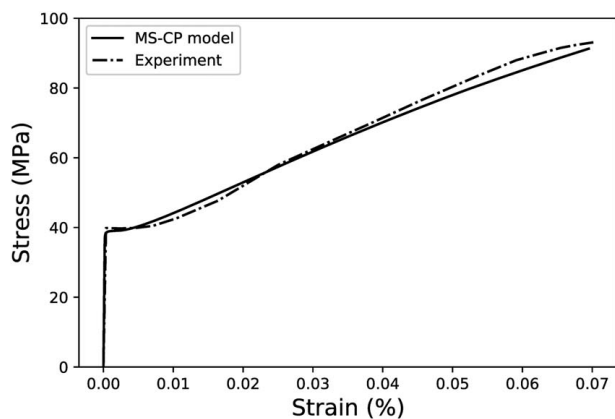


Fig. 2 Stress–strain curve comparison between models and experiments [56] for a nickel single crystal loaded in uniaxial tension along the $\langle -167 \rangle$ direction at a strain rate of $9 \times 10^{-5} \text{ s}^{-1}$ at 300 K

$$\Psi^\alpha = \frac{1}{2} \left\{ 1 + \operatorname{erf} \left[\frac{\tau^\alpha - \bar{\tau}}{\sqrt{2}\sigma} \right] \right\} \quad (7)$$

Here, $\bar{\tau}$ is the average activation stress, τ^α the slip system resolved shear stress, and σ the standard deviation of the activation stress. The density of activated sources can then be estimated assuming single slip as

$$\rho_{act}^\alpha = \rho^0 \Psi^\alpha \quad (8)$$

where ρ^0 is the total source density. The source activation rate $\dot{\rho}_+^\alpha$ can then be written as

$$\dot{\rho}_+^\alpha = \dot{\rho}_{act}^\alpha \frac{\bar{v}^\alpha}{l_s} \quad (9)$$

where l_s is the distance a loop must travel from a source before that source can emit another loop and \bar{v}^α is the average dislocation velocity, obtained on each slip system from Orowan's equation, i.e., $\dot{\gamma}^\alpha = \rho^\alpha b \bar{v}^\alpha$. Assuming the sources are spatially distributed according to a uniform random distribution, the probability of two loops annihilating in the channel can then be written as

$$p_{ann}^\alpha = C_n \gamma_s^{edge} (\rho_+^\alpha)^2 \quad (10)$$

where C_n is a normalization factor related to material density with units of m^3 and γ_s^{edge} is the annihilation distance for an emitted dislocation. Finally, the rate of Va concentration production is given by

$$\dot{C}_{Va+}^\alpha = \Phi_{ann} p_{ann}^\alpha \quad (11)$$

with Φ_{ann} an estimate of annihilation efficiency. As is observed in experiments, C_{Va} eventually saturates, requiring consideration of Va annihilation [63,64]. Therefore, we require a balance of Va production and annihilation, i.e.

$$\dot{C}_{Va}^\alpha = \dot{C}_{Va+}^\alpha - \dot{C}_{Va-}^\alpha \quad (12)$$

As a simple first-order approximation, we adopt the approach of Polak and Sauzay [58], where $\dot{C}_{Va-}^\alpha = A C_{Va}^\alpha$, with A being an adjustable model parameter. Overall, this model provides an estimate of C_{Va} for use in the MS-CP model.

The Va production model uses input information about the local state from the MS-CP model, e.g., τ^α , $\dot{\gamma}^\alpha$, and ρ^α . The source density is taken to be a value smaller than the initial dislocation density in the walls, and the critical bow out length is estimated from experimental results and simulations [65]. The value of A was motivated based on the experimentally observed saturation of the vacancy concentration [58] and was chosen based on parametric studies to generate reasonable vacancy concentrations. The source parameter σ is more difficult to obtain, as measurements do not exist. Further, discrete dislocation dynamics calculations which could potentially assess the source properties require prohibitively large dislocation densities. Due to these limitations, we consider choices for the source parameters as approximations and choose values consistent with Ref. [62]. The remaining model parameters are consistent to first order with values in similar work [58,62]. The parameters in this section are relevant for 300 K and are presented in Table 3.

3.2 Finite Element Model. The H transport and extended MS-CP models were implemented in the finite element software ABAQUS [66] through the user coding of the subroutines UMATHT and UMAT, respectively. Gobbi et al. [67] provide a detailed description of using the heat transfer user subroutine UMATHT in the solution of mass diffusion problems. ABAQUS uses these two user subroutines to simultaneously solve the

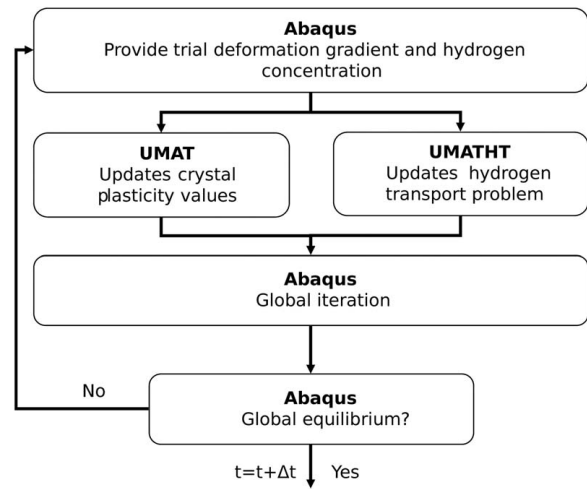


Fig. 3 Overview of coupled mechanical and H transport problem

coupled chemo-mechanical initial-boundary value problem as outlined in Fig. 3, which shows the logic for a single incremental step in the simulation.

The finite element model mesh was developed to represent a mesoscopic, blunt crack tip under generalized plane strain conditions. To maintain computational efficiency for the resource-intensive MS-CP crack tip problem, the mesh uses ABAQUS C3D8RT elements coupled with varying mesh density. These elements are eight-node thermally coupled bricks with reduced integration and hourglass control. Furthermore, the mesh is separated into near-field and far-field domains, with the MS-CP model applied to the near-field and a J_2 plasticity model representing macroscopic material behavior in the far-field. The mesh domain decomposition is shown in Fig. 4(a), where C_R is the crack tip radius. The boundary between the two domains, set as $150C_R$, was chosen to ensure the majority of intense plastic deformation remained in the MS-CP model domain. The J_2 mechanical response assumed simple linear elastic-plastic behavior described by an elastic modulus of 205 GPa, a post-yield tangent modulus of 800 MPa, and a yield stress of 100 MPa, appropriate for annealed nickel at room temperature. The H transport behavior of the J_2 model assumed isotropic diffusion described using the lattice diffusivity for nickel in Table 2. Here, we note that the simple J_2 model described above is adequate because the J_2 model domain is sufficiently distant from the crack tip and does not experience substantial plastic deformation. Consequently, dislocation-mediated H transport mechanisms are insignificant. The mesh density at the crack tip is shown in Fig. 4(b). It should be noted that the full domain shown in Fig. 4 is necessary since the MS-CP model exhibits both elastic and plastic anisotropy.

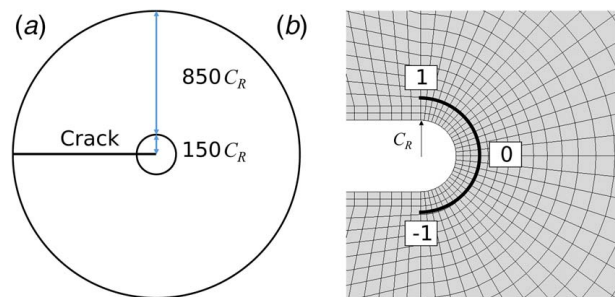


Fig. 4 (a) Domain decomposition into MS-CP and J_2 regions with radii of $150C_R$ and $850C_R$, respectively and (b) mesh used near the crack tip with the measurement location for subsequent plots marked by the thick black line.

Table 3 Va concentration evolution parameters for nickel

$\bar{\tau}$	σ	ρ^0	l_s	C_n	Φ_{ann}	A
100 MPa	20 MPa	10^{10} source/ m^2	5×10^{-9} m	$4b^3 m^3$	1000	0.1

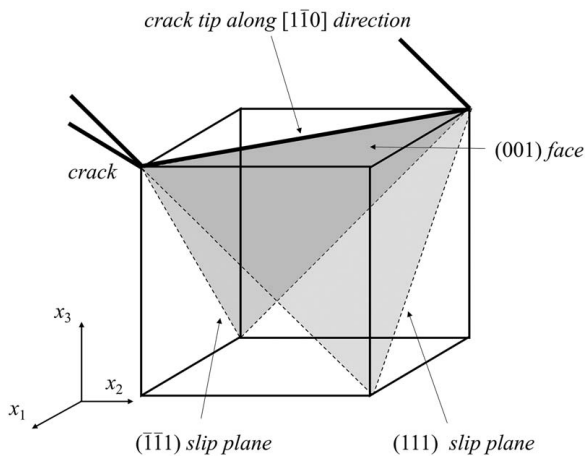


Fig. 5 Crack orientation with respect to the FCC unit cell

The initial-boundary value problem consists of the simultaneous solution of the coupled mechanical and chemical initial-boundary conditions. The mechanical boundary condition uses a Mode I K-field applied as a time-dependent boundary condition at the outer boundary of Fig. 4(a), corresponding to the Irwin singular elastic field for plane strain conditions at a crack tip [68]. The applicability of using crack tip boundary conditions with initially blunted cracks was determined for each load tested by ensuring the initial crack radius fell below the blunted crack tip radius predicted by linear elastic fracture mechanics [69]. For all simulations except for the notch acuity study, a crack tip radius of $8 \mu\text{m}$ is assumed, and the crack length is assumed to greatly exceed the crack tip radius. Lastly, all simulations are performed at 300 K.

The crack is oriented with respect to the FCC lattice such that the crack plane is (001) and the crack front aligns with the $[1\bar{1}0]$ direction. This corresponds to the crack plane being parallel to an FCC unit cell face and the crack tip lying along an FCC unit cell face diagonal, as shown in Fig. 5.

The chemical problem prescribes a constant H concentration C_0 of 1.24 mol/m^3 (8.17×10^{-6} dimensionless concentration) at the crack surface, corresponding to the surface material being in equilibrium with H_2 gas at 1 atm [49,70]. The material is H-free initially, facilitating solution of a transient transport problem. The boundary conditions are representative of pressurized H containment vessels assuming rapid equilibration of the surface H with gaseous H.

The combination of a constant H concentration at the crack surface, relatively low diffusion coefficients in FCC crystals, and a sufficiently large domain size preclude a focus on steady-state

solutions. Furthermore, the crystal orientation dependence of the MS-CP model increases the complexity of simulating and interpreting H transport and trapping. Accordingly, analyses will concentrate on the heterogeneity of fields and parametric comparisons pertaining to the transient solution. To assist in the analysis, many figures (i.e., Figs. 6, 7, and 11) plot the variable of interest around the crack tip along a semi-circular curve to capture spatial heterogeneity. In these plots, the x -axis corresponds to the thick black line in Fig. 4(b) where the axis is normalized so that 1, 0, and -1 correspond to the top, tip, and bottom of the initially semi-circular, blunted crack tip. The x -axis normalization is used instead of angles to prevent confusion with measurements regarding slip system activity with respect to the crack plane. The chosen extraction location is taken as a characteristic example of behavior manifested in the crack tip region of intense plasticity and note that the trends observed at this location are representative of behavior throughout the crack tip region. Furthermore, when “averaged” results are referenced, the average is taken with respect to values extracted along this curve. Overall, we consider variation of coupled fields around the periphery of the crack tip as opposed to the radial distance, focusing on the orientation dependence of fields arising from elastic and plastic crystal anisotropies.

4 Results

4.1 Hydrogen Transport and Trapping. The coupling between H transport and trapping is key to the proposed model. As shown by Sofronis and McMeeking [17], the presence of traps lowers the “effective” or so-called “observed” diffusivity of H, D_{obs} . Note that this “observed” diffusivity, derived mathematically from the H transport formulation, differs from the effective diffusivity that incorporates pipe diffusion presented in Eq. (6). The derivation of D_{obs} , previously reported in literature [17,24], makes clear the role of strong H traps in decreasing the rate of H diffusion, i.e.

$$\frac{D_{obs}}{D} = \frac{C_L}{C_L + C_T(1 - \theta_T)} \quad \text{for } \theta_L \ll 1 \quad (13)$$

where D is the diffusivity of mobile H, θ_T is the fraction of occupied immobilizing traps, and θ_L is the fraction of occupied lattice sites. For the current model, $D = D_{eff}$, $C_T = C_{HVa}$, and $\theta_T = \theta_{HVa}$. Equation (13) shows that the H diffusion rate is lowest when all traps are empty and highest when all traps are filled. In other words, empty H traps serve as sinks for mobile H that lowers the observed diffusivity. Therefore, the transient distribution of H depends on the production of Va traps as well as the ability of mobile H to move to those traps.

The production of strain-generated Va depends on the activity of dislocation-mediated slip. As such, the Va trap distribution ahead of

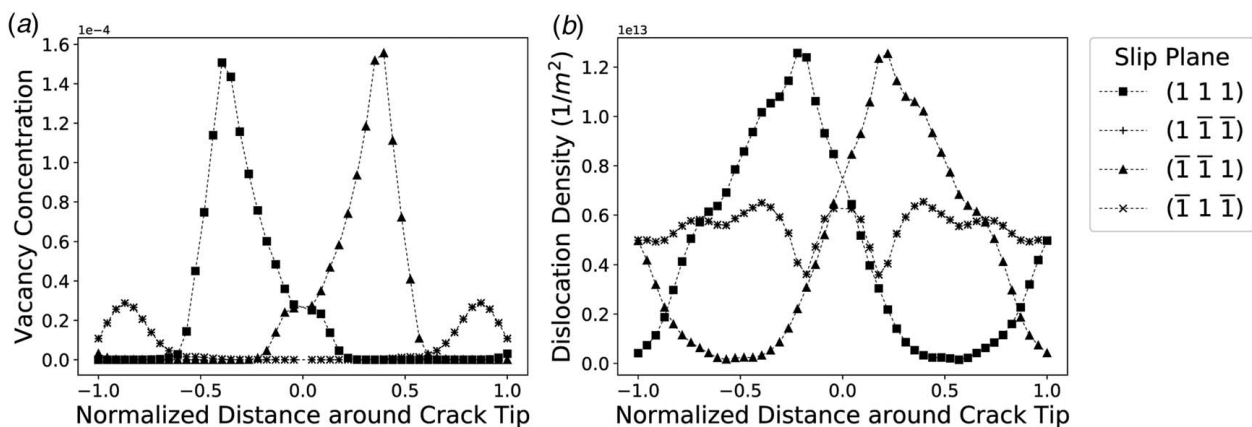


Fig. 6 (a) Dimensionless C_{Va} and (b) dislocation density on the four FCC slip plane families at final mode I stress intensity factor of $20 \text{ MPa}\cdot\text{m}^{1/2}$. Abscissa in both plots corresponds to thick black line demarcated in Fig. 4(b).

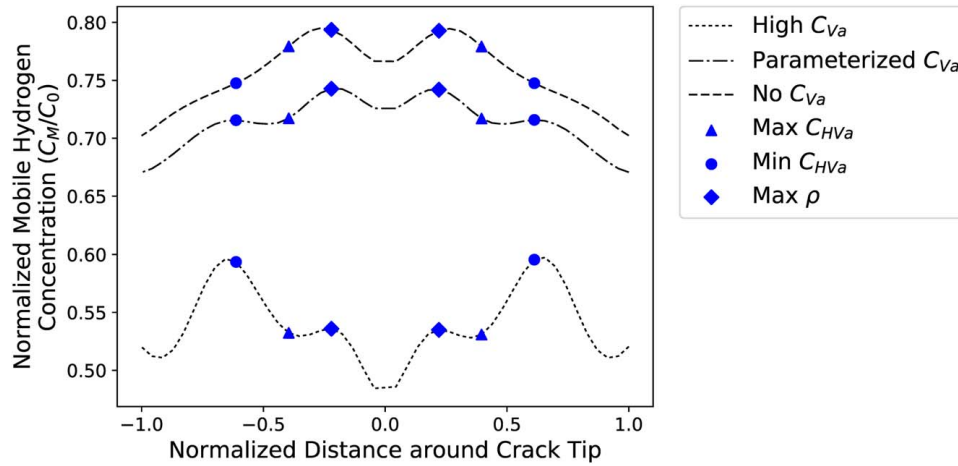


Fig. 7 C_M/C_0 distributions for varying Va defect concentrations. Abscissa corresponds to thick black line demarcated in Fig. 4(b).

the crack tip is expected to depend on the orientation of the crack plane and crack front relative to the crystal. Va generation was studied by loading the crack to a stress intensity factor of $20 \text{ MPa}\cdot\text{m}^{1/2}$ over 200 s, after which C_{Va} was extracted around the crack tip, as shown in Fig. 6(a). In this plot, C_{Va} is separated into four curves based on the FCC slip plane activity that generated the Va: (111), $(\bar{1}\bar{1}\bar{1})$, $(\bar{1}\bar{1}1)$, or $(1\bar{1}\bar{1})$. From inspection of Fig. 6(a), the slip planes that dominate the Va production are (111) and $(\bar{1}\bar{1}\bar{1})$. The slip system activity agrees with the results of Rice [71], who showed the primary active slip systems in the prescribed crack orientation belong to the (111) and $(\bar{1}\bar{1}\bar{1})$ slip planes, shown in Fig. 5. Furthermore, while the results in Fig. 6 pertain to a fixed radial distance from the blunt crack tip surface, the Va field contours extend into the material at angles of approximately 55 deg from the crack plane, closely matching the theoretical 54.7 deg angle expected from the orientation of the (111) and $(\bar{1}\bar{1}\bar{1})$ slip planes.

The same dislocation slip activity responsible for the production of Va is also expected to enhance H transport. The dislocation density around the crack tip is shown in Fig. 6(b). Similar to C_{Va} in Fig. 6(a), the largest dislocation density is achieved along the (111) and $(\bar{1}\bar{1}\bar{1})$ slip planes. However, unlike C_{Va} , the dislocation density experiences a more uniform distribution around the crack tip. The more uniform dislocation density about the crack tip is primarily due to intense regions of localized slip promoting cross slip to less active slip systems [72]. This phenomenon, while influencing the dislocation density, does little to increase C_{Va} as the intense slip system shearing rates remain localized on the (111) and $(\bar{1}\bar{1}\bar{1})$ slip planes. A shift will be expected upon dislocation source saturation or sufficient forest dislocation entanglements.

Figure 6 shows the distribution of Va and dislocations ahead of a crack tip, hypothesized to influence the distribution of H due to trapping and transport, respectively. While the values shown in Fig. 6 are for a specific crack tip load, the trends are consistent throughout the simulation. As a final note, the Va concentrations shown in Fig. 6 are of the same order of magnitude as those computed using large-scale molecular dynamics simulations in iron [39] and are consistent with observations related to hydrogen enhanced strain induced vacancy generation [15,16].

The same loading used to generate the point and line defects shown in Fig. 6 was used to investigate the competition between H transport and trapping. The normalized mobile H concentration, C_M/C_0 , around the crack tip is plotted in Fig. 7. For the simulations shown in this plot, the Va production was suppressed entirely (No C_{Va}), allowed to evolve according to the proposed model (Parameterized C_{Va}), and artificially elevated by a factor of 10 (High C_{Va}). Furthermore, the locations of maximum and minimum C_{HVa} and maximum dislocation density ρ from Fig. 6 are plotted on the C_M/C_0 curves to assist in the analysis.

In accordance with Eq. (13), increasing levels of Va production limit the amount of mobile H available for transport. The dotted curve, corresponding to the elevated Va production case, has appreciably lower C_M compared with the other cases. Conversely, suppressing the Va trap production entirely produces the dashed line which exhibits the largest C_M available for transport. This observation highlights the role that Va traps play in decreasing C_M .

Superimposing the maximum and minimum values of the internal defect populations shown in Fig. 6 on the mobile H curves in Fig. 7 highlights a shift in dominant mechanism upon varying defect population intensities. We start by examining the two Va production extremes: no Va production and artificially increased Va production. The dashed curve, corresponding to no production of Va, is dominated by dislocation-mediated transport mechanisms as evidenced by the maximum mobile H concentration coinciding with ρ^{max} (diamond marker). The combined effect of high shearing rates and large dislocation densities enhance the transport of H on active slip planes. In short, the increase in effective diffusivity due to pipe diffusion and the additional flux due to sweeping of H by dislocations are most evident in the absence of Va traps.

Examination of the other extreme, that of high Va production, shows altogether different results. The dotted curve, corresponding to high Va production, is dominated by strain-generated trapping behavior as evidenced by the maximum C_M coinciding with C_{HVa}^{min} (circle marker). In other words, the absence of Va traps produces a relative increase in C_M . Furthermore, the dotted curve has a local minimum and maximum corresponding to C_{HVa}^{max} (triangle marker) and ρ^{max} (diamond marker), respectively. Here, the slight increase in C_M (diamond marker) is due to the additional dislocation-mediated transport mechanisms mitigating the effect of the strong Va traps in the same localized area (triangle marker).

Understanding the two extremes of Va production guides the interpretation of the dot-dashed curve in Fig. 7, corresponding to the parameterized Va production model. Here, the distribution of C_M is not dominated by either transport or trapping, but rather a competition between the two. The local maxima of the dot-dashed curve closely aligns with the locations of ρ^{max} (diamond marker) and C_{HVa}^{min} (circle marker), previously shown to enable H transport. On the other hand, the local minima of the dot-dashed curve closely aligns with C_{HVa}^{max} (triangle marker), previously shown to suppress H transport. The overarching takeaway from the result shown in Fig. 7 is the competition between transport and trapping in the transient distribution of C_M ahead of the crack tip. The increased mobility of H due to the dislocation-mediated pipe diffusion and dislocation sweeping mechanisms is offset by the production of strain-generated Va. The solution provides valuable insight into the relationship between various model components, pertinent in the analysis of later results.

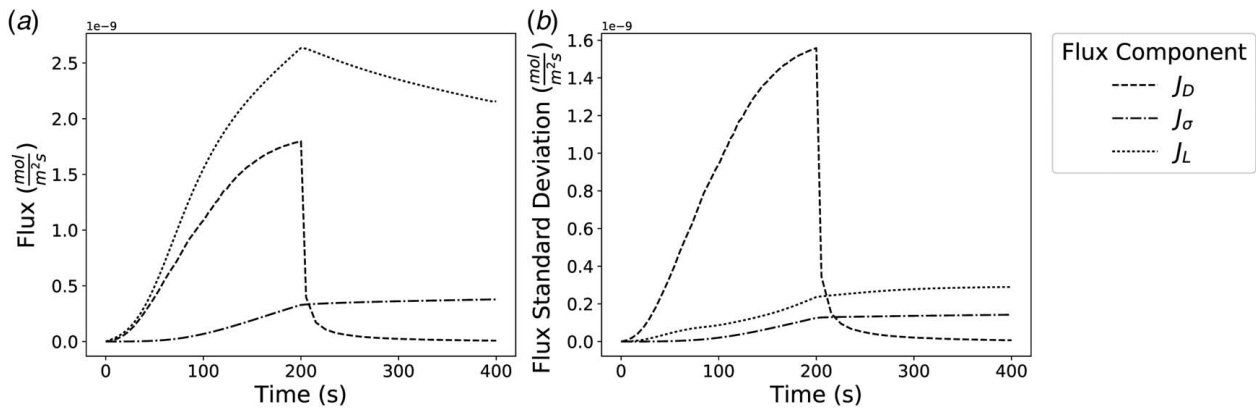


Fig. 8 (a) Average flux components and (b) standard deviation of flux components as a function of time. Loading occurs from 0 to 200 s up to the maximum mode I stress intensity factor of $20 \text{ MPa}\cdot\text{m}^{1/2}$. Load held constant from 200 to 400 s.

The result in Fig. 7 shows a snapshot of the transient solution, but the trends are consistent throughout the loading. Deviations from these trends are expected upon adequate slip system hardening and C_{HVa} saturation. With regard to strain hardening, the most active slip systems undergo localized hardening due to forest dislocation entanglements and dislocation source exhaustion, triggering secondary slip systems activation [73,74]. The defect concentrations will evolve to accommodate the newly activated slip planes and ultimately influence the distribution of H ahead of the crack tip. In accordance with experiments, C_{Va} is expected to saturate [63,64]. Once Va production has ceased, the transport-suppressing Va sinks are expected to saturate, restoring the ability of H to be transported further from the crack tip. With enough time, the distribution is expected to approach that of the dashed line in Fig. 7, corresponding to no Va traps, or equivalently, completely saturated H-Va complexes. Depending on the mechanism of hydrogen embrittlement suspected to be active, however, the defect concentration of interest may shift from C_M to C_{HVa} . In this regard, while the C_M distributions may be identical upon sufficient time for diffusion, the C_{HVa} distributions created during the transient solution remains vastly different between the two scenarios.

As a final exploration of the H transport and trapping model, the time-dependent aspects were investigated. For this purpose, the crack was loaded to $20 \text{ MPa}\cdot\text{m}^{1/2}$ over 200 s, after which the load was held constant for 200 additional seconds. This loading history results in the cessation of meaningful dislocation and Va generation once the load is held constant and remnant viscoplastic effects terminate. To facilitate study of the dominant transport mechanisms, the average contribution of each flux component magnitude about the crack tip is plotted as a function of simulation time in Fig. 8(a). In this case, the “average contribution” refers to the average flux magnitude measured at the location demarcated by the thick black line in Fig. 4(b). As a measure of the spatial heterogeneity of the flux terms, the standard deviation of each flux component magnitude about the crack tip is plotted as a function of simulation time in Fig. 8(b). Similar to the average contribution, the standard deviation refers to the standard deviation of the flux components measured at the location demarcated by the thick black line in Fig. 4(b).

Considering Fig. 8(a), the lattice and dislocation flux components dominate during the loading portion of the simulation, i.e., 0–200 s. This is consistent with the results of Sun et al. [75], who experimentally determined that the effect of hydrostatic stress gradient driven flux, J_σ , is less important in the presence of straining. All three flux components are dependent on the applied load level and increase accordingly with dislocation generation and substructure development during loading. Once the load is held constant, however, significant dislocation emission from the crack tip ceases and the flux component due to dislocation sweeping, J_D , drops to zero as expected. While dislocation emission from the crack tip effectively stops, the dislocation substructure developed over the loading

regime remains. In other words, while J_D becomes inconsequential, the contribution of pipe diffusion through an enhanced diffusivity, D_{eff} , is still active. Note the relatively constant magnitudes of J_σ and J_L once loading has ceased. The slight decrease in J_L when the load is held constant is due to decreasing driving force for lattice diffusion as H continues to diffuse ahead of the crack tip. If the load was held longer, the H concentration gradient would continue to decrease and J_σ would begin to dominate, creating a relative increase in the concentration of mobile H at the location of maximum hydrostatic stress as previously demonstrated [17,24].

Figure 8(b) shows the standard deviation of the flux component magnitudes about the crack tip. The standard deviation is plotted as a measure of spatial heterogeneity, i.e., a higher standard deviation corresponds to more localized flux activity. As can be seen, J_D clearly exhibits the most intense local activity when compared with either J_σ or J_L . While all flux components depend on dislocation activity, J_D also has a functional dependence on the slip system shearing rates, which remain highly localized on the (111) and ($\bar{1}\bar{1}\bar{1}$) slip planes, increasing the heterogeneity of J_D during loading. Conversely, J_σ and J_L depend on the dislocation substructure density and associated pipe diffusion. As previously mentioned, the cross slip ahead of the crack results in more homogeneous dislocation density evolution and subsequent dislocation substructure development about the crack tip. The overall takeaway from Fig. 8(b) is the increasing spatial heterogeneity of H flux in the loading regime and the subsequent return to more homogenous H flux upon cessation of loading.

The total H distribution is driven by heterogeneity in both transport and trapping mechanisms. The results in Fig. 8, pertaining to H transport, provide insight into the differences between the proposed H transport model and classical formulations like those of Sofronis and McMeeking [17]. The results of Sofronis and McMeeking [17] suggest that lattice H preferentially segregates to the location of maximum hydrostatic stress with H being substantially trapped at regions of high plastic strain. Indeed, a similar result is achieved with the current model if dislocation-mediated transport is suppressed and crystal orientation accounted for. Introduction of both dislocation-mediated transport and Va-mediated trapping increase the spatial heterogeneity of the resulting H distribution compared with the results of Sofronis and McMeeking [17] as shown by the large standard deviation of the dislocation flux component shown in Fig. 8(b) (transport) and the C_{Va} distribution (trapping) shown in Fig. 6(a). As suggested by the experimental results of Sun et al. [75], capturing the enhanced spatial heterogeneity of H distributions associated with crystallographic orientation becomes essential at sufficiently small length scales.

4.2 Loading Rate Effects. The viscoplastic nature of the crystal plasticity model is able to capture strain rate dependent

material behavior, and H transport and trapping behavior has also been shown to be dependent on strain rate [76]. To investigate the influence of load rate, the crack tip was loaded to a stress intensity factor of $20 \text{ MPa}\cdot\text{m}^{1/2}$ over a range of times corresponding to loading rates of 0.08, 0.13, and $0.4 \text{ MPa}\cdot\text{m}^{1/2}/\text{s}$. Decreased loading rates clearly result in longer loading times, and while longer loading times naturally result in more time for diffusion to occur, important observations can still be made.

Va produced via the annihilation of dislocation loops bowing out from dislocation dense walls [58] depend on the slip system shearing rates, accumulation of dislocation emission sites, and buildup of Va over time. The functional dependence of the Va production model on both slip system shearing rates and the evolution of loop emission sites creates a competition between the load rate and the overall time elapsed, as seen in Fig. 9(a). In this plot, C_{Va} ahead of the crack tip is plotted as a function of simulation time for the three loading rates. The curves end at different points because the faster loading rates achieve the maximum load of $20 \text{ MPa}\cdot\text{m}^{1/2}$ quicker. As can be seen, the maximum C_{Va} is obtained for a loading rate of $0.13 \text{ MPa}\cdot\text{m}^{1/2}/\text{s}$. While faster loading rates correspond to increased slip system shearing rates and high rates of Va generation, there is not sufficient time to accumulate the loop emission sites or Va required to match the C_{Va} produced at $0.13 \text{ MPa}\cdot\text{m}^{1/2}/\text{s}$. Below the $0.13 \text{ MPa}\cdot\text{m}^{1/2}/\text{s}$ loading rate, however, the slip system shearing rates are not adequate to produce appreciable dislocation emission despite the longer overall time required to achieve the maximum load.

As discussed in Sec. 4.1 and demonstrated in Fig. 7, Va provide a saturable trap for mobile H, ultimately limiting H transport. Based solely on Fig. 9(a), the loading rate of $0.13 \text{ MPa}\cdot\text{m}^{1/2}/\text{s}$ would be

expected to demonstrate the least intense mobile H concentration ahead of the crack tip due to the elevated Va concentration generated. The time-dependent nature of diffusion, however, mitigates the effect of the enhanced Va production as more H is able to diffuse to and saturate Va traps. The average observed diffusivity, as defined in Eq. (13), is shown in Fig. 9(b). Here, D_{obs} is plotted as a function of simulation time for the different loading rates. The decrease in D_{obs} with increasing strain rate aligns with previous thinking regarding the strain rate dependence of H transport and trapping [26]. From this plot, it can be seen that despite generating the highest Va concentration, the loading rate of $0.13 \text{ MPa}\cdot\text{m}^{1/2}/\text{s}$ does still offer a relatively favorable environment for further H transport.

The dislocation-mediated transport mechanisms assisting H transport are influenced by loading rate. The flux of mobile dislocations that sweep H is directly linked to slip system shearing rates through Orowan's equation. Furthermore, the increased loading rate will enhance dislocation activity and subsequent development of dislocation substructure that increase the effective diffusivity via pipe diffusion. The average magnitudes of the dominant flux components, J_D and J_L , are plotted in Fig. 10 as a function of simulation time for the three loading rates. The magnitude and rate of both J_D and J_L increase with higher loading rates, consistent with the higher levels of dislocation flux and dislocation density.

The results shown in Figs. 9 and 10 demonstrate the strain rate dependence of the coupled model. The overall manifestation of these dependencies in the transient solution of the H transport model results in the C_M/C_0 distributions around the crack tip shown in Fig. 11(a). In this plot, C_M/C_0 is plotted for a range of loading rates at the maximum load of $20 \text{ MPa}\cdot\text{m}^{1/2}$. Here, higher loading rates are represented by darker curves.

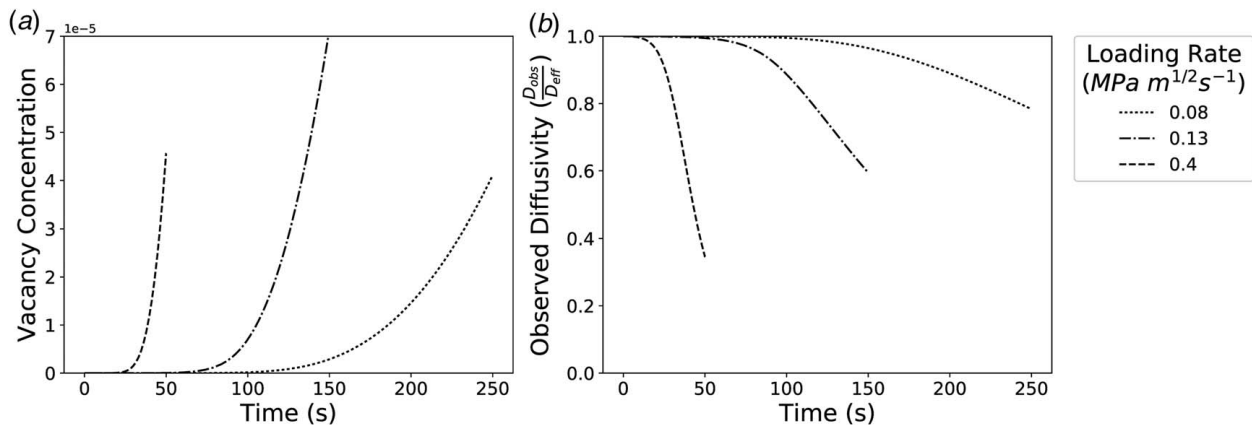


Fig. 9 (a) Dimensionless C_{Va} and (b) D_{obs} ahead of the crack tip as a function of simulation time until the maximum applied stress intensity factor of $20 \text{ MPa}\cdot\text{m}^{1/2}$ is reached

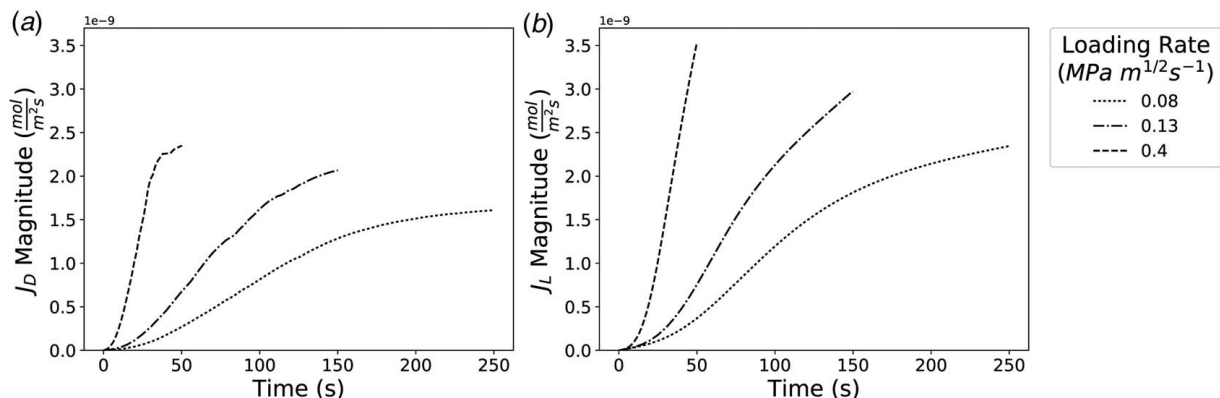


Fig. 10 (a) Average magnitude of dislocation flux J_D and (b) average lattice flux J_L magnitude ahead of the crack tip evolving as a function of simulation time to the maximum load of $20 \text{ MPa}\cdot\text{m}^{1/2}$

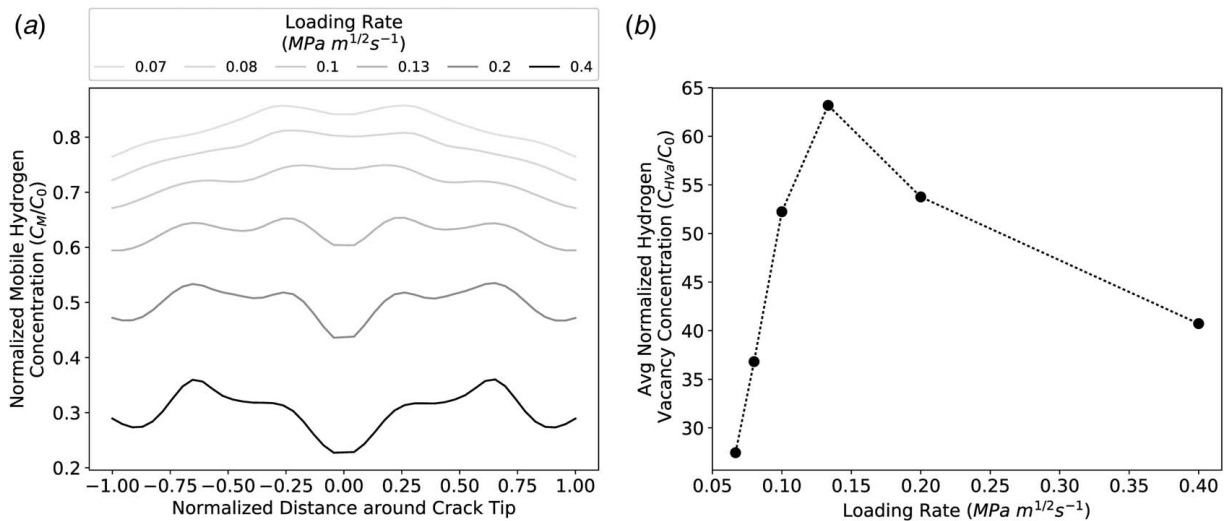


Fig. 11 (a) C_M/C_0 as a function of distance around the crack tip and loading rate to the maximum stress intensity factor of $20 \text{ MPa}\cdot\text{m}^{1/2}$ and (b) C_{HVa}/C_0 as a function of loading rate at $20 \text{ MPa}\cdot\text{m}^{1/2}$. Abscissa in (a) corresponds to thick black line demarcated in Fig. 4(b).

As seen in Fig. 11(a), higher loading rates result in more heterogeneous H distributions. At higher loading rates, the curve shape approaches that of the high Va production case shown in Fig. 7. As discussed, the distribution in this case is dominated by the distribution of Va. The increased heterogeneity is due to the two-fold influence of increased Va production at faster loading rates and the decreased time available for mobile H to diffuse to and saturate the Va traps. Conversely, the trends of the slower loading rate curves approach that of the suppressed Va production case shown in Fig. 7. The distribution of H in this case is dominated by the distribution of transport enhancing dislocation populations.

Overall, the strain rate sensitivity of the transport and trapping model manifests itself through a transition in dominant mechanism from transport-dominated at low strain rates to trapping-dominated at high strain rates. While this transition seems to occur monotonically with loading rate, the defect distributions ahead of the crack tip demonstrate more complicated behavior. The competition between higher loading rates (producing high Va concentrations) and the time required for H to diffuse to those Va traps produces rather non-intuitive evolution of fields. If one assumes a hydrogen embrittlement mechanism similar to the hydrogen enhanced strain induced vacancy mechanism, the H concentration of interest shifts from C_M to C_{HVa} . For the range of loading rates considered, the maximum average C_{HVa} is observed at the intermediate load rate of $0.13 \text{ MPa}\cdot\text{m}^{1/2}/\text{s}$, as seen in Fig. 11(b). The complex trapping

behavior as a result of varying the strain rate highlights the non-intuitive, complex nature of H transport and trapping in the presence of strain-generated traps. This provides some insight into why the spatial distribution of H concentration is difficult to estimate without using coupled approaches.

4.3 Notch Severity. Crack blunting occurs in ductile materials in order to relieve the stress concentration experienced at the crack tip [69]. Regardless of the active crack propagation mechanism(s), e.g., void coalescence or cleavage through work hardened material, the crack will experience variations in acuity as it propagates in the material [77]. For void coalescence, the eventual linking of voids generated via internal necking results in a crack increment with more intense notch acuity [78]. For cleavage, dislocation emission exhaustion results in crack advances upon sufficient crack tip blunting, resulting in a sharp crack [79,80]. Overall, the variation in crack tip acuity throughout a crack growth process is expected to change and influence the transport and trapping of H.

The influence of notch acuity on the transport and trapping of H was studied by loading the crack to $40 \text{ MPa}\cdot\text{m}^{1/2}$ over 200 s for a range of notch root radius: 8, 18, 28, and $38 \mu\text{m}$. The applicability of Irwin's singular elastic field for plane strain conditions at a sharp crack tip decreases with increasing crack radii, and, to ensure validity, the notch root radii were chosen to fall below the blunted crack

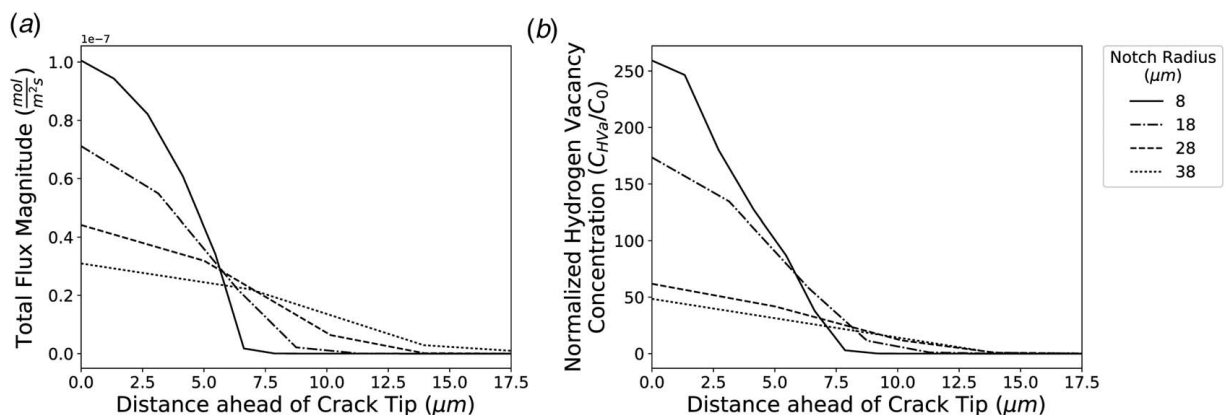


Fig. 12 (a) Total H flux magnitude and (b) normalized C_{HVa} as a function of distance away from the crack tip along the (111) slip plane

tip radius predicted by linear elastic fracture mechanics (40 μm). Furthermore, the mesh density and overall domain size were scaled with notch root radii. While the same loading was applied to each crack radius, the volume available to accommodate plastic deformation decreases, ultimately resulting in H transport and trapping behavior variation. The variation in response due to various crack radii can be considered to be an analog to the variation in response due to crack tip blunting and the associated change in mechanical response.

The influence of notch blunting was investigated by comparing behavior localization. Characteristic model parameters capturing H transport and trapping behavior as a function of distance away from the crack tip along the (111) slip plane are shown in Fig. 12. While the results shown in Fig. 12 pertain to the (111) slip plane, the same trends are demonstrated around the crack tip, albeit to a lesser extent due to the relative inactivity of the slip planes at those locations. The trends exhibited in Fig. 12 reveal that for both the total H flux magnitude and normalized C_{HVa} , “sharper” cracks result in more intense localization. Considering this to capture transport and trapping behavior, respectively, sharper cracks can be considered to localize H transport and trapping behavior. The results in Fig. 12 suggest that the ability of the crack tip to blunt during deformation would mitigate the accumulation of defects ahead of the crack tip. Depending on the hydrogen embrittlement mechanisms assumed to be active, this could have real consequences for the propagation of the crack in the material.

5 Discussion and Conclusions

Specific characteristics of the proposed H transport and trapping model have been explored, i.e., the competition between H transport and trapping in highly strained regions, the influence of load rate on the model, and the localization behavior associated with blunted cracks of various radii. The results presented provide insights into how this model can be used to support exploration of hydrogen embrittlement. The coupling of the H transport and trapping and MS-CP material models enables the exploration of orientation dependent behavior. While the results presented here were limited to a symmetric crystal orientation relative to the crack plane and crack front, the alignment of transport and trapping behavior with active slip planes demonstrates the ability of the model to capture heterogeneous behavior. When compared with classic approaches, such as J_2 plasticity approaches, the proposed model enhances predictive capability by modeling the heterogeneity of both H transport and trapping. In the current model, the transient distribution of lattice H and steady-state distribution of trapped H is dependent on slip system behavior and associated plastic strain heterogeneity. The dependence of most proposed H embrittlement mechanisms on H-related defect concentrations implies that capturing the influence of crystallographic orientation is highly relevant to modeling H embrittlement.

This study has proposed a more complete H transport model that extends previous formulations [17,24] to include dislocation-mediated transport and various modes of trapping of H. The model was exercised on a mesoscopic crack tip under a variety of load scenarios, exhibiting appreciable sensitivity to variations in loading rate and severity of the crack tip radius. Near the tip of a blunted crack, the proposed H transport model has been found to produce

- distributions of Va traps that depend on slip system activity and loading schedule,
- distributions of both mobile and trapped H that depend on slip system activity and loading schedule,
- a competition between trapping- and transport-dominated H distributions, and
- descriptions of point and line defect concentrations in the material that facilitate exploration of a range of previously proposed hydrogen embrittlement mechanisms.

In particular, the results presented here point to the importance of accounting for the enhanced trapping and transport of H via dislocation-mediated mechanisms. The defect concentrations generated ahead of the crack tip are expected to localize deformation behavior and cause a self-sustaining cycle of defect generation and strain localization. Overall, the distributions of H and associated defect concentrations near the crack tip are difficult to probe experimentally, and the proposed H transport model provides a computational pathway for exploring the wide variety of H embrittlement mechanisms proposed in literature.

While the results presented pertain to monotonic loading, some preliminary observations can be made regarding model response under cyclic loading of the cracked body. The enhanced trapping and transport formulations depend on sustained plastic flow in order to generate dislocations and vacancies. At the tip of a crack, the cyclic plastic strains can be quite significant, giving rise to an important role for vacancy generation due to dislocation-dislocation interactions and dislocation-enhanced H transport. Future work will address these aspects.

Mechanical constitutive equations with a functional dependence on the concentration of H-related defects are expected to further influence the transport and transport behavior of H in the material. Modification of the MS-CP model in the context of H embrittlement has been briefly explored before by Castelluccio et al. [81]. In that work, the modification of the constitutive model resulted in an increased initial yield strength followed by a region of decreased work hardening when compared with the H-free model. It is difficult to know a priori how this coupling will change transport and trapping behavior because of the complicated interplay between the transport model and slip behavior. Regardless, the exploration of model forms presented here will guide the interpretation of model results when the mechanical constitutive equations include full dependence on H-related point and line defect concentrations, a focus of future work.

Acknowledgment

The authors are grateful for the support from the Naval Nuclear Laboratory, operated by Fluor Marine Propulsion, LLC for the US Naval Reactors Program. Additionally, the crack tip mesh generation code developed by contract monitor Dr. Benjamin Anglin was key in the model implementation. Furthermore, the authors also appreciate the support of the Carter N. Paden, Jr. Distinguished Chair in Metals Processing at Georgia Tech.

Conflict of Interest

There are no conflicts of interest.

Data Availability Statement

The authors attest that all data for this study are included in the paper. Data provided by a third party listed in Acknowledgment.

Appendix

A brief description of the MS-CP model is included here for completeness. For complete details on the model, please refer to Ref. [55]. The flow rule describing the shearing rate of dislocations on slip system α follows a Kocks-Argon-Ashby type relation [47], i.e.

$$\dot{\gamma}^\alpha = \rho_m^\alpha \bar{l} v_G \exp\left(\frac{-\Delta G(\tau_{eff}^\alpha)}{k_B T}\right) \text{sgn}(\tau^\alpha - B^\alpha) \quad (\text{A1})$$

where ρ_m^α is the density of mobile screw dislocations, \bar{l} is the mean free path of a dislocation between obstacle bypass events, b is the Burgers vector, and v_G is an estimate of the attempt frequency.

Furthermore, ΔG is the required energy to bypass short-range obstacles, τ_{eff}^α is the effective stress, τ^α is the local slip system resolved shear stress, B^α is the directional intragranular back stress, k_B is the Boltzmann constant, and T is the absolute temperature. For face-centered cubic crystals, $\alpha = 1, 2, \dots, 12$ specifies each of the available octahedral slip systems.

Quantity τ_{eff}^α is the effective stress that drives barrier bypass at the slip system level and is given by $\tau_{eff}^\alpha = (|\tau^\alpha - B^\alpha| - S^\alpha)$. Here, S^α is the nondirectional athermal threshold stress and $\langle g \rangle$ corresponds to the Macaulay bracket notation, i.e., $\langle g \rangle = 0$ if $g \leq 0$ and $\langle g \rangle = g$ otherwise. The activation energy, ΔG , associated with dominant short-range barriers to thermally assisted dislocation motion, is expressed as

$$\Delta G = F_0 \left(1 - \left[\frac{\tau_{eff}^\alpha}{s_t^0 C_{44}} \right]^p \right)^q \quad (A2)$$

where F_0 is the activation energy, and p and q are profiling parameters. Parameter s_t^0 is the athermal limit of thermal slip resistance at 0 K, and C_{44} and $C_{44@0K}$ are the shear modulus at temperature T and 0 K, respectively. This relation must reflect the statistical distribution of barriers at the mesoscale via F_0 and profile parameters p and q .

The threshold stress, S^α , accounts for the intrinsic lattice friction, the stress required to bow out a dislocation, and the dislocation-dislocation self-interactions that result from collinear dislocations in pile-ups. The overall contribution of these three mechanisms can be expressed additively as

$$S^\alpha = S_0^\alpha + \alpha_{LE} \frac{\mu b}{2d_{struct}} + \mu b (A_{ii} \rho_m^\alpha)^{1/2} \quad (A3)$$

where α_{LE} is a factor that depends on the dislocation line energy, μ is the polycrystal-averaged shear modulus, A_{ii} is the self-interaction coefficient from the full latent hardening matrix, and d_{struct} is the characteristic dimension of dislocation wall substructures. Intrinsic lattice friction S_0^α is quite small for FCC systems, about 4 MPa in this case, and is dominated by the short range barriers associated with thermal slip resistance s_t^0 .

The back stress accounts for the directional internal stress developed due to heterogeneity of plastic deformation within dislocation substructures, ensuring the largely plastic strain in dislocation channels maintains compatibility with the largely elastic strain in dislocation substructure walls. The back stress superimposes on the applied resolved shear stress to form the effective directional over stress. Assuming an Eshelby-type inclusion formulation [82], the

back stress rate can be expressed as

$$\dot{B}^\alpha = \frac{f_w}{1 - f_w} \frac{2\mu(1 - 2S_{1212}^\alpha)}{1 + 4S_{1212}^\alpha \mu f_{Hill}^\alpha} \dot{\gamma}^\alpha \quad (A4)$$

where f_{Hill}^α is the instantaneous macroscopic plastic deformation tangent, f_w is the volume fraction of dislocation substructure walls, and S_{1212}^α is a component of the Eshelby tensor component [83].

Determination of the dislocation substructure parameters relies on experimentally observed similitude characteristics. Following previous works [84,85], the characteristic dislocation substructure length scale is determined via

$$d_{struct} = \frac{K_{struct} \mu b}{\max(|\tau^\alpha|)} \quad (A5)$$

where K_{struct} is the constant of similitude and the max function in the denominator returns the maximum slip system level resolved shear stress in the volume of interest. The mean free path for dislocation glide is evaluated as

$$\bar{l} \approx l_{struct} = \eta d_{struct} \quad (A6)$$

where η is a parameter determining the aspect ratio of dislocation substructures. For example, $\eta = 1$ corresponds to dislocation cells while $\eta = 50$ corresponds to more elongated substructures such as dislocation veins. For cyclic loading, η is determined by evaluating cyclic plastic strain ranges. In the current study, where specific focus is placed on monotonic loading, this value is assigned a constant value.

The last dislocation substructure parameter to be described is the volume fraction of dislocation dense substructure walls. Here, a phenomenological relationship is leveraged from prior work [86] to define the dislocation substructure wall volume fraction, i.e.

$$f_w = f_{inf} + (f_0 - f_{inf}) \exp\left(\frac{-0.5\gamma^{max}}{g_p}\right) \quad (A7)$$

where f_{inf} , f_0 , and g_p are constants that can be estimated by careful substructure characterization using tools such as transmission electron microscopy. Lastly, γ^{max} is the maximum shear strain over all slip systems.

The mobile screw dislocation density evolution on slip system α is a result of the competition between dislocation multiplication, annihilation, and cross slip. Following prior work [87,88], the overall expression for the dislocation density evolution can be

Table 4 Parameters related to the MS-CP model for Ni at room temperature

Direct parameters										
v_G	b	C_{11}	C_{12}	C_{44}	$C_{44@0K}$	μ				
10^{12} s^{-1}	$2.5 \times 10^{-10} \text{ m}$	249 GPa	155 GPa	114 GPa	127.6 GPa	80.6 GPa				
Parameters related to atomistic mechanisms										
F_0	s_t^0	p	q	γ_s^{edge}	γ_s^{screw}	S_0	A_{ii}	α_{LE}	V_0^{CS}	ϕ_{cs}
0.985 eV	100 MPa	0.9	1.5	3 nm	13 nm	4 MPa	0.1	1	$10^3 b^3$	0.5
Parameters related to mesoscale dislocation structures										
K_{struct}	k_{multi}	f_{inf}	f_0	g_p	η					
12	1	0.06	0.25	1.7	1					
Reference initial values for Ni										
ρ_m^α	d_{struct}	f_0^w								
10^{10} m^{-2}	10 μm	0.25								

written as

$$\dot{\rho}_m^\alpha = \dot{\rho}_{multi}^\alpha - \dot{\rho}_{annih}^\alpha + \dot{\rho}_{cs}^{|\zeta \rightarrow \alpha} - \dot{\rho}_{cs}^{|\alpha \rightarrow \zeta} \quad (A8)$$

The multiplication rate is defined as

$$\dot{\rho}_{multi}^\alpha = \frac{k_{multi}}{bl_{struct}} |\dot{\gamma}^\alpha| \quad (A9)$$

where k_{multi} is a constant that modulates the dislocation multiplication. The annihilation rate for monotonic loading is defined as

$$\dot{\rho}_{annih}^\alpha = \frac{2y_s^{edge}}{b} \rho_m^\alpha |\dot{\gamma}^\alpha| \quad (A10)$$

where y_s^{edge} is the annihilation distance for edge dislocations. A second annihilation term formulated by Castelluccio and McDowell [55] to account for anelastic dislocation annihilation upon unloading is dropped in Eq. (A10) as focused is placed on monotonic loading.

The cross slip term follows a probabilistic formulation from previous work [89], but considers a local shear stress that accounts for dislocation substructure shielding, i.e.

$$\dot{\rho}_{cs}^{|\alpha \rightarrow \zeta} = v_G^{cs} \varphi_{cs} \rho_m^\alpha \exp\left(-V_{cs} \frac{\tau_{III} - |\tau^\zeta - B^\zeta|}{k_B T}\right) \quad (A11)$$

$$\dot{\rho}_{cs}^{|\zeta \rightarrow \alpha} = v_G^{cs} \varphi_{cs} \rho_m^\zeta \exp\left(-V_{cs} \frac{\tau_{III} - |\tau^\alpha - B^\alpha|}{k_B T}\right) \quad (A12)$$

where v_G^{cs} , τ_{III} , φ_{cs} , and V_{cs} are the characteristic cross slip frequency, critical cross slip stress at the onset of stage III hardening, cross slip efficiency, and cross slip activation volume, respectively. Indices ζ and α denote collinear slip systems that permit cross slip. The parameters used in the MS-CP model for Ni are provided in Table 4 with full justification provided in Ref. [55].

References

- [1] Johnson, W. H., 1875, "On Some Remarkable Changes Produced in Iron and Steel by the Action of Hydrogen and Acids," *Nature*, **11**(281), pp. 393.
- [2] Myers, S. M., Baskes, M., Birnbaum, H., Corbett, J. W., DeLeo, G., Estreicher, S., Haller, E. E., Jena, P., Johnson, N. M., and Kirchheim, R., 1992, "Hydrogen Interactions with Defects in Crystalline Solids," *Rev. Mod. Phys.*, **64**(2), pp. 559–617.
- [3] Barthélémy, H., 2012, "Hydrogen Storage—Industrial Perspectives," *Int. J. Hydrogen Energy*, **37**(22), pp. 17364–17372.
- [4] Gangloff, R. P., and Somerday, B. P., 2012, *Gaseous Hydrogen Embrittlement of Materials in Energy Technologies: The Problem, Its Characterisation and Effects on Particular Alloy Classes*, Elsevier, New York.
- [5] Popov, K., and Nechai, E., 1967, "Theory of Hydrogen Embrittlement of Metals," *Soviet Materials Science: A Transl. of Fiziko-khimicheskaya mekhanika materialov/Academy of Sciences of the Ukrainian SSR*, **3**(6), pp. 459–473.
- [6] Ghermaoui, I., Oudriss, A., Metsue, A., Milet, R., Madani, K., and Feaugas, X., 2019, "Multiscale Analysis of Hydrogen-Induced Softening in FCC Nickel Single Crystals Oriented for Multiple-Slips: Elastic Screening Effect," *Sci. Rep.*, **9**(1), pp. 1–10.
- [7] Beacham, C., 1972, "A New Model for Hydrogen-Assisted Cracking (Hydrogen Embrittlement)," *Metall. Trans.*, **3**, pp. 437–451.
- [8] Birnbaum, H. K., and Sofronis, P., 1994, "Hydrogen-Enhanced Localized Plasticity—A Mechanism for Hydrogen-Related Fracture," *Mater. Sci. Eng. A*, **176**(1–2), pp. 191–202.
- [9] Lynch, S., 1979, "Hydrogen Embrittlement and Liquid-Metal Embrittlement in Nickel Single Crystals," *Scr. Metall.*, **13**(11), pp. 1051–1056.
- [10] Lynch, S., 1988, "Environmentally Assisted Cracking: Overview of Evidence for an Adsorption-Induced Localised-Slip Process," *Acta Metall.*, **36**(10), pp. 2639–2661.
- [11] Lynch, S., 1989, "Metallographic Contributions to Understanding Mechanisms of Environmentally Assisted Cracking," *Metallography*, **23**(2), pp. 147–171.
- [12] Petch, N., and Stables, P., 1952, "Delayed Fracture of Metals Under Static Load," *Nature*, **169**(4307), pp. 842–843.
- [13] Pfeil, L. B., 1926, "The Effect of Occluded Hydrogen on the Tensile Strength of Iron," *Proc. R. Soc. Lond. A*, **112**(760), pp. 182–195.
- [14] Troiano, A., 1973, "General Keynote Lecture, Hydrogen in Metals," *Proc. Int. Conf. on the Effects of Hydrogen on Materials Properties and Selection and Structural Design*, Champion, PA, Sept. 23–27, 1973.
- [15] Hatano, M., Fujinami, M., Arai, K., Fujii, H., and Nagumo, M., 2014, "Hydrogen Embrittlement of Austenitic Stainless Steels Revealed by Deformation

- Microstructures and Strain-Induced Creation of Vacancies," *Acta Mater.*, **67**, pp. 342–353.
- [16] Nagumo, M., 2004, "Hydrogen Related Failure of Steels—A New Aspect," *Mater. Sci. Technol.*, **20**(8), pp. 940–950.
- [17] Sofronis, P., and McMeeking, R. M., 1989, "Numerical Analysis of Hydrogen Transport Near a Blunting Crack Tip," *J. Mech. Phys. Solids*, **37**(3), pp. 317–350.
- [18] Charles, Y., Nguyen, H. T., and Gaspérini, M., 2017, "Comparison of Hydrogen Transport Through Pre-Deformed Synthetic Polycrystals and Homogeneous Samples by Finite Element Analysis," *Int. J. Hydrogen Energy*, **42**(31), pp. 20336–20350.
- [19] Hassan, H. U., Govind, K., and Hartmaier, A., 2019, "Micromechanical Modelling of Coupled Crystal Plasticity and Hydrogen Diffusion," *Philos. Mag.*, **99**(1), pp. 92–115.
- [20] Hüter, C., Shanthraj, P., McEniry, E., Spatschek, R., Hickel, T., Tehranchi, A., Guo, X., and Roters, F., 2018, "Multiscale Modelling of Hydrogen Transport and Segregation in Polycrystalline Steels," *Metals*, **8**(6), p. 430.
- [21] Ilin, D. N., Sainnier, N., Olive, J.-M., Abgrall, R., and Aubert, I., 2014, "Simulation of Hydrogen Diffusion Affected by Stress-Strain Heterogeneity in Polycrystalline Stainless Steel," *Int. J. Hydrogen Energy*, **39**(5), pp. 2418–2422.
- [22] Miresmaeili, R., Sainnier, N., Notsu, H., Olive, J.-M., and Kanayama, H., 2010, "One-Way Coupled Crystal Plasticity-Hydrogen Diffusion Simulation on Artificial Microstructure," *J. Comput. Sci. Technol.*, **4**(2), pp. 105–120.
- [23] Sainnier, N., Awane, T., Olive, J.-M., Matsuoka, S., and Murakami, Y., 2011, "Analyses of Hydrogen Distribution Around Fatigue Crack on Type 304 Stainless Steel Using Secondary Ion Mass Spectrometry," *Int. J. Hydrogen Energy*, **36**(14), pp. 8630–8640.
- [24] Dadfarnia, M., Martin, M. L., Nagao, A., Sofronis, P., and Robertson, I. M., 2015, "Modeling Hydrogen Transport by Dislocations," *J. Mech. Phys. Solids*, **78**, pp. 511–525.
- [25] Murakami, Y., Kanezaki, T., Mine, Y., and Matsuoka, S., 2008, "Hydrogen Embrittlement Mechanism in Fatigue of Austenitic Stainless Steels," *Metall. Mater. Trans. A*, **39**(6), pp. 1327–1339.
- [26] Hashimoto, M., and Latanision, R., 1988, "The Role of Dislocations During Transport of Hydrogen in Hydrogen Embrittlement of Iron," *Metall. Trans. A*, **19**(11), pp. 2799–2803.
- [27] Cortes, R., Valiente, A., Ruiz, J., Caballero, L., and Toribio, J., 1997, "Finite-Element Modeling of Stress-Assisted Hydrogen Diffusion in 316L Stainless Steel," *Mater. Sci.*, **33**(4), pp. 491–503.
- [28] Van Leeuwen, H., 1974, "The Kinetics of Hydrogen Embrittlement: A Quantitative Diffusion Model," *Eng. Fract. Mech.*, **6**(1), pp. 141–161.
- [29] Love, G., 1964, "Dislocation Pipe Diffusion," *Acta Metall.*, **12**(6), pp. 731–737.
- [30] San Marchi, C., Somerday, B. P., and Robinson, S. L., 2007, "Permeability, Solubility and Diffusivity of Hydrogen Isotopes in Stainless Steels at High Gas Pressures," *Int. J. Hydrogen Energy*, **32**(1), pp. 100–116.
- [31] Nair, S., Jensen, R., and Tien, J., 1983, "Kinetic Enrichment of Hydrogen at Interfaces and Voids by Dislocation Sweep-in of Hydrogen," *Metall. Trans. A*, **14**(2), pp. 385–393.
- [32] Schuster, G., and Altstetter, C., 1983, "Fatigue of Stainless Steel in Hydrogen," *Metall. Trans. A*, **14**(10), pp. 2085–2090.
- [33] Wang, Y., Connétable, D., and Tanguy, D., 2015, "Hydrogen Influence on Diffusion in Nickel From First-Principles Calculations," *Phys. Rev. B*, **91**(9), p. 094106.
- [34] Wen, M., Fukuyama, S., and Yokogawa, K., 2004, "Hydrogen-Affected Cross-Slip Process in FCC Nickel," *Phys. Rev. B*, **69**(17), p. 174108.
- [35] Angelo, J. E., Moody, N. R., and Baskes, M. I., 1995, "Trapping of Hydrogen to Lattice Defects in Nickel," *Modell. Simul. Mater. Sci. Eng.*, **3**(3), pp. 289–307.
- [36] Tanguy, D., Wang, Y., and Connétable, D., 2014, "Stability of Vacancy-Hydrogen Clusters in Nickel From First-Principles Calculations," *Acta Mater.*, **78**, pp. 135–143.
- [37] Myers, S., Nordlander, P., Besenbacher, F., and Nørskov, J., 1986, "Theoretical Examination of the Trapping of Ion-Implanted Hydrogen in Metals," *Phys. Rev. B*, **33**(2), pp. 854–863.
- [38] Hirth, J., and Lothe, J., 1982, *Theory of Dislocations*, Wiley, New York.
- [39] Li, S., Li, Y., Lo, Y.-C., Neeraj, T., Srinivasan, R., Ding, X., Sun, J., Qi, L., Gumbsch, P., and Li, J., 2015, "The Interaction of Dislocations and Hydrogen-Vacancy Complexes and Its Importance for Deformation-Induced Proto Nano-Voids Formation in α -Fe," *Int. J. Plast.*, **74**, pp. 175–191.
- [40] Kays, W. M., 2012, *Convective Heat and Mass Transfer*, Tata McGraw-Hill Education, New York.
- [41] Hart, E., Hoffman, R., and Turnbull, D., 1957, "Self-Diffusion in Dilute Binary Solid Solutions—II," *Acta Metall.*, **5**(2), pp. 74–76.
- [42] Chen, Y., and Schuh, C. A., 2007, "Geometric Considerations for Diffusion in Polycrystalline Solids," *J. Appl. Phys.*, **101**(6), p. 063524.
- [43] Frank, F., 1950, *Report of the Symposium on the Plastic Deformation of Crystalline Solids*, Carnegie Institute of Technology, Pittsburgh, p. 150.
- [44] McLellan, R. B., 1979, "Thermodynamics and Diffusion Behavior of Interstitial Solute Atoms in Non-Perfect Solvent Crystals," *Acta Metall.*, **27**(10), pp. 1655–1663.
- [45] Tien, J., Thompson, A. W., Bernstein, I., and Richards, R. J., 1976, "Hydrogen Transport by Dislocations," *Metall. Trans. A*, **7**(6), pp. 821–829.
- [46] Fukai, Y., 2003, "Formation of Superabundant Vacancies in M–H Alloys and Some of Its Consequences: A Review," *J. Alloys Compd.*, **356–357**, pp. 263–269.
- [47] Kocks, U. F., Argon, A. S., and Ashby, M. F., 1975, "Thermodynamics and Kinetics of Slip," *Prog. Mater. Sci.*, **19**, pp. 1–281.
- [48] Mughrabi, H., 1979, "Microscopic Mechanisms of Metal Fatigue," *Proceedings of the 5th International Conference on Strength of Metals and Alloys*, Aachen, Germany, Vol. 3, pp. 1615–1638.

- [49] Louthan, M., Jr, Donovan, J., and Caskey, G., Jr, 1975, "Hydrogen Diffusion and Trapping in Nickel," *Acta Metall.*, **23**(6), pp. 745–749.
- [50] Lee, S.-M., and Lee, J.-Y., 1986, "The Trapping and Transport Phenomena of Hydrogen in Nickel," *Metall. Trans. A*, **17**(2), pp. 181–187.
- [51] Chen, D., 2018, Personal Communication.
- [52] Liang, Y., Ahn, D., Sofronis, P., Dodds, R., Jr, and Bammann, D., 2008, "Effect of Hydrogen Trapping on Void Growth and Coalescence in Metals and Alloys," *Mech. Mater.*, **40**(3), pp. 115–132.
- [53] Zheng, H., Rao, B., Khanna, S., and Jena, P., 1997, "Electronic Structure and Binding Energies of Hydrogen-Decorated Vacancies in Ni," *Phys. Rev. B*, **55**(7), pp. 4174–4181.
- [54] Myers, S., Richards, P., Wampler, W., and Besenbacher, F., 1989, "Ion-Beam Studies of Hydrogen-Metal Interactions," *J. Nucl. Mater.*, **165**(1), pp. 9–64.
- [55] Castelluccio, G. M., and McDowell, D. L., 2017, "Mesoscale Cyclic Crystal Plasticity With Dislocation Substructures," *Int. J. Plast.*, **98**, pp. 1–26.
- [56] Yagodzinsky, Y., Saukkonen, T., Kilpeläinen, S., Tuomisto, F., and Hänninen, H., 2010, "Effect of Hydrogen on Plastic Strain Localization in Single Crystals of Austenitic Stainless Steel," *Scr. Mater.*, **62**(3), pp. 155–158.
- [57] Polák, J., and Man, J., 2014, "Fatigue Crack Initiation—The Role of Point Defects," *Int. J. Fatigue*, **65**, pp. 18–27.
- [58] Polák, J., and Sauzay, M., 2009, "Growth of Extrusions in Localized Cyclic Plastic Straining," *Mater. Sci. Eng. A*, **500**(1–2), pp. 122–129.
- [59] Differt, K., and Essmann, U., 1993, "Dynamical Model of the Wall Structure in Persistent Slip Bands of Fatigued Metals I. Dynamical Model of Edge Dislocation Walls," *Materials Science and Engineering: A*, **164**(1–2), pp. 295–299.
- [60] Essmann, U., Gösele, U., and Mughrabi, H., 1981, "A Model of Extrusions and Intrusions in Fatigued Metals I. Point-Defect Production and the Growth of Extrusions," *Philos. Mag. A*, **44**(2), pp. 405–426.
- [61] Essmann, U., and Mughrabi, H., 1979, "Annihilation of Dislocations During Tensile and Cyclic Deformation and Limits of Dislocation Densities," *Philos. Mag. A*, **40**(6), pp. 731–756.
- [62] Davoudi, K. M., and Vlassak, J. J., 2018, "Dislocation Evolution During Plastic Deformation: Equations vs. Discrete Dislocation Dynamics Study," *J. Appl. Phys.*, **123**(8), p. 085302.
- [63] Schafner, E., Steiner, G., Korznikova, E., Kerber, M., and Zehetbauer, M., 2005, "Lattice Defect Investigation of ECAP-Cu by Means of X-Ray Line Profile Analysis, Calorimetry and Electrical Resistometry," *Mater. Sci. Eng. A*, **410–411**, pp. 169–173.
- [64] Ungár, T., 2006, "Subgrain Size-Distributions, Dislocation Structures, Stacking-and Twin Faults and Vacancy Concentrations in SPD Materials Determined," *Materials Science Forum*, **503–504**, pp. 133–140.
- [65] Xu, S., Xiong, L., Chen, Y., and McDowell, D. L., 2016, "An Analysis of Key Characteristics of the Frank-Read Source Process in FCC Metals," *J. Mech. Phys. Solids*, **96**, pp. 460–476.
- [66] ABAQUS, F., 2009, *software V6. 9*, Simulia Corp., Providence, RI, Simulia, Inc.
- [67] Gobbi, G., Colombo, C., Miccoli, S., and Vergani, L., 2019, "A Fully Coupled Implementation of Hydrogen Embrittlement in FE Analysis," *Adv. Eng. Software*, **135**, p. 102673.
- [68] Irwin, G., 1968, "Linear Fracture Mechanics, Fracture Transition, and Fracture Control," *Eng. Fract. Mech.*, **1**(2), pp. 241–257.
- [69] Anderson, T. L., 2017, *Fracture Mechanics: Fundamentals and Applications*, CRC Press, Boca Raton, FL.
- [70] Ebisuzaki, Y., Kass, W., and O'keeffe, M., 1967, "Diffusion and Solubility of Hydrogen in Single Crystals of Nickel and Nickel—Vanadium Alloy," *J. Chem. Phys.*, **46**(4), pp. 1378–1381.
- [71] Rice, J. R., 1987, "Tensile Crack Tip Fields in Elastic-Ideally Plastic Crystals," *Mech. Mater.*, **6**(4), pp. 317–335.
- [72] Bitzek, E., and Gumbsch, P., 2013, "Mechanisms of Dislocation Multiplication at Crack Tips," *Acta Mater.*, **61**(4), pp. 1394–1403.
- [73] Alcalá, J., Očenášek, J., Nowag, K., Esqué-de los Ojos, D., Ghisleni, R., and Michler, J., 2015, "Strain Hardening and Dislocation Avalanches in Micrometer-Sized Dimensions," *Acta Mater.*, **91**, pp. 255–266.
- [74] Kiener, D., and Minor, A., 2011, "Source Truncation and Exhaustion: Insights From Quantitative In Situ TEM Tensile Testing," *Nano Lett.*, **11**(9), pp. 3816–3820.
- [75] Sun, S., Shiozawa, K., Gu, J., and Chen, N., 1995, "Investigation of Deformation Field and Hydrogen Partition Around Crack Tip in FCC Single Crystal," *Mater. Sci. Eng. A*, **26**(3), pp. 731–739.
- [76] Doshida, T., and Takai, K., 2014, "Dependence of Hydrogen-Induced Lattice Defects and Hydrogen Embrittlement of Cold-Drawn Pearlitic Steels on Hydrogen Trap State, Temperature, Strain Rate and Hydrogen Content," *Acta Mater.*, **79**, pp. 93–107.
- [77] Ritchie, R. O., 1999, "Mechanisms of Fatigue-Crack Propagation in Ductile and Brittle Solids," *Int. J. Fract.*, **100**(1), pp. 55–83.
- [78] Taggart, R., Wahi, K., and Beeuwkes, R., 1976, *Properties Related to Fracture Toughness*, V. Weiss and W. Warke, eds., ASTM International, West Conshohocken, PA.
- [79] Farkas, D., Duranduru, M., Curtin, W., and Ribbens, C., 2001, "Multiple-Dislocation Emission From the Crack Tip in the Ductile Fracture of Al," *Philos. Mag. A*, **81**(5), pp. 1241–1255.
- [80] Puttick, K., 1959, "Ductile Fracture in Metals," *Philos. Mag.*, **4**(44), pp. 964–969.
- [81] Castelluccio, G. M., Geller, C. B., and McDowell, D. L., 2018, "A Rationale for Modeling Hydrogen Effects on Plastic Deformation Across Scales in FCC Metals," *Int. J. Plast.*, **111**, pp. 72–84.
- [82] Eshelby, J. D., 1957, "The Determination of the Elastic Field of an Ellipsoidal Inclusion, and Related Problems," *Proc. R. Soc. London, A*, **241**(1226), pp. 376–396.
- [83] Mura, T., 2013, *Micromechanics of Defects in Solids*, Springer Science & Business Media, Dordrecht, The Netherlands.
- [84] Sauzay, M., and Kubin, L. P., 2011, "Scaling Laws for Dislocation Microstructures in Monotonic and Cyclic Deformation of FCC Metals," *Prog. Mater. Sci.*, **56**(6), pp. 725–784.
- [85] Kuhlmann-Wilsdorf, D., 1962, "A New Theory of Work Hardening in Crystals," *Trans. Met. Soc.*, **218**, p. 962.
- [86] Estrin, Y., Toth, L., Molinari, A., and Bréchet, Y., 1998, "A Dislocation-Based Model for All Hardening Stages in Large Strain Deformation," *Acta Mater.*, **46**(15), pp. 5509–5522.
- [87] Arsenlis, A., and Parks, D. M., 2002, "Modeling the Evolution of Crystallographic Dislocation Density in Crystal Plasticity," *J. Mech. Phys. Solids*, **50**(9), pp. 1979–2009.
- [88] Patra, A., and McDowell, D. L., 2012, "Crystal Plasticity-Based Constitutive Modelling of Irradiated BCC Structures," *Philos. Mag.*, **92**(7), pp. 861–887.
- [89] Kubin, L. P., Canova, G., Condat, M., Devincere, B., Pontikis, V., and Bréchet, Y., 1992, "Dislocation Microstructures and Plastic Flow: A 3D Simulation," *Solid State Phenom.*, **23–24**, pp. 455–472.